ADVANCED MATERIALS

Structural Analysis of Self-Assembling Nanocrystal Superlattices**

By Zhong Lin Wang*

1. Introduction

Nanophase and nanoparticle materials are a new generation of advanced materials that are expected to exhibit unusual chemical and physical properties different from those of either the bulk materials or single atoms.[1] Engineering of nanophase materials and devices is of vital interest in electronics,[2] semiconductors and optics,[3] catalysis,[4] ceramics,[5] and magnetism.[6,7] The unique properties of nanophase materials are determined by their atomic scale structures, particularly the structures of interfaces and surfaces. The role played by particle size is comparable, in some cases, to the particle chemical composition, thus adding another flexible parameter to the design and control of their behavior.

In fact, studies of small particles and catalysis particles have been a focused area of scientific research for decades. But it is only recently that a new ideal has begun to be realized. Nanoparticles and the physical and chemical functional specificity and selectivity they possess, naturally suggest them as ideal building blocks for two- and three-dimensional cluster self-assembled superlattice structures (in powder, thin film, and solid bulk form), in which the particles behave like well-defined molecular matter, arranged with long-range translational and even orientational order.[8] Well-defined ordered solids prepared from tailored nanocrystalline building blocks provide new opportunities to optimize and enhance the properties and performance of the materials. This is a new initiative in research on *cluster engineered* materials.

Research has successfully fabricated self-assembled passivated nanocrystal superlattices (NCSs) or nanocrystal arrays (NCAs) of metal, semiconductor, and oxide clusters, which are a new form of materials of fundamental interest and technological importance. There are four key steps to developing these materials: controlled preparation of size and shape selected nanoparticles, control of the self-assembly process to produce large well-ordered NCSs, structural characterization, and modeling the dynamic behavior of the system. Indeed, understanding and optimizing the structures of the NCSs is an important step towards a systematic exploration of the nature of patterned superstructures assembled from such building units and formulation and implementation of methods for designing and controlling such novel assembled materials and their operational characteristics.

This article focuses on the structural analysis of NCSs with an emphasis on electron microscopy related techniques. The objective is to present an in-depth understanding of the nature of the 2D and 3D assembly of nanocrystals and the methodology of their analysis. This article is anticipated to serve as a general guide to solving the structural problems associated with nanocluster engineered crystalline materials.

2. Self-Assembling Nanocrystal Superlattices

Self-assembled arrays involve self-organization of size-selected nanoclusters encapsulated in protective compact organic coatings into monolayers, thin films, and superlattices. A key step in this process is the fabrication of size and shape controlled NCAs that have the potential to grow to a size large enough for technological applications. Colloidal chemistry, or soft chemistry, has played a powerful role in this process. Self-organization of nanoparticles is a new route to the synthesis of superlattice materials—solid, periodic arrays built using nanocrystals as building blocks,[8–12] achieved by preparing size and shape selected nanocrystals using colloid chemistry and then using self-assembly as a means of joining them together (Fig. 1).[13] The macroscopic properties of the NCS is determined not only by the properties of each individual particle but by the coupling/interaction between nanocrystals interconnected and isolated by a monolayer of thin organic molecules. By changing the length of the molecular chains, quantum transitions and insulator-to-conductor transitions could be introduced.

NCSs are characterized by unprecedented size uniformity and translational and even orientational order, created through a multistage processing strategy involving self-assembly, annealing, etching of defects, reversible passiva-

[*] Prof. Z. L. Wang
School of Materials Science and Engineering
Georgia Institute of Technology
Atlanta, GA 30332-0245 (USA)

[**] I am grateful to my collaborators, Drs. R. L. Whetten, S. A. Harfenist, I. Vezmar, M. M. Alvarez, and S. Murthy, who kindly supplied the nanocrystal specimens used for the TEM characterizations described here. Thanks also go to Professor M. A. El-Sayed and Dr. T. S. Ahmadi for providing the Pt nanocrystals, Professor Uzi Landman for many stimulating discussions about the bundling effect and to Dr. Jinsong Yin for his contribution and technical assistance. This work was supported in part by the NSF grant DMR-9632823.

  0935-9648/98/0101-0013 $ 17.50+.50/0

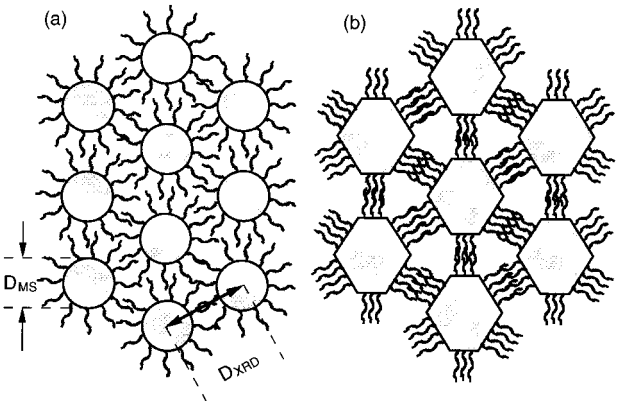

Fig. 1. Schematics showing self-assembled passivated nanocrystal superlattices of spherical (a) and faceted (b) particles.

tion by self-assembled monolayers, and macroscopic size separation of the resulting assemblies. Although there are numerous techniques for preparing metal clusters, most of the current research on self-assembled metal particles is concentrated on Au,[8,14,15] Ag,[12,16,17] and Ag_2S.[18,19] Particles that can be self-assembled are usually smaller than 10 nm in size; it is in this size range that many exciting and unusual physical properties are enhanced. The nanocrystal thin films reported here are formed primarily on a solid substrate via the self-assembly of nanocrystals. An alternative technique for forming monolayer nanocrystal thin films is at the liquid surface using Langmuir–Blodgett films, which has shown great potential in the synthesis and assembly of nanocrystals. A recent review by Fendler and Meldrum[20] provides a comprehensive coverage of this technique.

Out of all of the systems, the gold particle is probably the most advanced molecular crystal system that has been widely studied. Gold nanocrystals can be prepared either by an aerosol technique[21] or the soft chemistry technique,[22,23] in which metal particles grow as $AuCl_4^-$ is reduced at the oil–water interface in the presence of an alkylthiolate surfactant (SR, where R = n-C_nH_{2n+1}, n = 4, 6, 8, 12…) and a reducing agent (thiolate). The surfactant specifies compact and ordered monolayer passivation of the thiolate over the nanocrystal surface. The thiolate serves not only as a protective layer for the particles, which prevents direct contact between the particles and consequent collapse of the structure, but also provides interparticle bonding. The strength of this bond characterizes the structural stability and the maximum operational temperature the materials can withstand. The core size of the particles can be controlled by changing the gold-to-thiolate ratio.[24,25] Recent studies have shown that the size of the Au core and the length of the thiolate are the two parameters that determine the 3D crystal structure of the nanocrystal assembly (i.e., phase diagram). The studies of Andres et al.[26] have demonstrated that the alkylthiolate can be replaced by aryl dithiol or aryl diisonitrile molecules to form covalently bonded NCAs with enhanced structural stability and mechanical strength.

Synthesis and studies of semiconductor nanocrystals are of vital practical importance for many optoelectronic applications.[3] The most interesting phenomena associated with semiconductors are the quantum-dot effect, surface states, and charge transport.[27] The properties of nanocrystals appear to be very different from bulk crystals if they approach atomic dimensions or ionic diffusion lengths, electronic elastic and inelastic mean free path lengths, or correlation and screening lengths. A recent report by Murray et al.[28] showed that the 3D hexagonal close-packed (*hcp*) and face-centered cubic (*fcc*) assembly of CdSe nanocrystals, prepared using a two-solvent recrystallization method, can result in crystalline superlattices as large as 50 μm.

The preparation of cobalt NCSs is being studied in our laboratory.[29] Naturally, magnetic particles smaller than 10 nm are usually superparamagnetic and they do not aggregate because each particle is a single magnetic domain. Thus, it is possible to form self-assembled NCSs. Recently, a permanent magnetic moment was observed in a self-assembled array of Co particles (with sizes < 8 nm) by aligning them in a magnetic field during assembly.[29] Co particles in the size range 20–80 nm tend to form chain-like structures,[30] and can form long one-dimensional chains,[31–34] indicating a strong preference for forming cluster engineered arrays of Co particles. A recent report by Zhang and Budnick[35] included some X-ray diffraction data that

Zhong Lin (ZL) Wang is currently an Associate Professor and Director of the Electron Microscopy Facility at the Georgia Institute of Technology, Atlanta, Georgia, USA. He received his B.Sc. in physics from Xidian University (previously Northwestern Telecommunication Engineering Institute), Xi'an, China in 1982 and his Ph.D. in physics from Arizona State University in 1987. Between 1987 and 1994, Dr. Wang carried out research at the Cavendish Laboratory (University of Cambridge, UK), the Oak Ridge National Laboratory, and the National Institute of Standards and Technology. Dr. Wang has extensive research interests in transmission electron microscopy and associated techniques. He is particularly interested in the microstructure and property relationships of advanced materials and is currently focusing on functional and smart materials, magnetic materials, and patterned nanocrystal superlattices and thin films.

0935-9648/98/0101-0014 $ 17.50+.50/0

ADVANCED MATERIALS

supported the formation of a single-crystal-like aggregate of Sm_2Fe_{17} magnetic clusters by an external magnetic field.

Oxide particles with a narrow size distribution can also form ordered NCSs. Recently, monodisperse tetrahedral nanocrystals of CoO were prepared and formed large-area self-assembled monolayers, in which size and phase selection were performed using a magnetic field.[36] A decade ago Bentzon et al.[37,38] demonstrated the *hcp* packing of α-Fe_2O_3 nanoparticles (antiferromagnet) prepared by decomposition of $Fe(CO)_5$ in a mixture of decalin and Sarkosyl-O.[39] This was a significant advance that proved the experimental feasibility of forming ordered NCSs of oxide particles. Dispersed ε-Fe_3N fine particles synthesized by a vapor–liquid chemical reaction between $Fe(CO)_5$ and ammonia resulted in a narrow size distribution, with the formation of nicely locally ordered monolayer arrays.[40]

Periodic packing of nanocrystals is different from the 3D packing of atoms in several aspects. First, to an excellent approximation atoms are spherical, while nanoparticles can be faceted polyhedra, thus the 3D packing of particles can be critically affected by their shape and size. Second, the atom size is fixed, but the size of nanoparticles can vary slightly, although their size distribution is very narrow. Finally, atomic bonding occurs between outershell (valence) electrons to form ionic, covalent, or metallic bonds, or mixtures of these. In most cases the interatomic distance is fixed, while the bonding between nanoparticles is generated by a passivating thiolate surfactant whose length is controllable, thus the ratio of particle size to interparticle distance is adjustable. This is a parameter likely to determine the 3D packing of the nanoparticles. The tunable internanocrystal spacing permits control over interparticle interactions, giving rise to novel tunable structural, optical, and transport properties.

3. Atomic-Scale Structure of Nanoparticles

Studies of the atomic-scale structure of nanoparticles have been carried out for many years and the literature is vast. High-resolution transmission electron microscopy (HRTEM) has played a vital role as it is the only technique that allows real-space imaging of the atomic distribution in nanoparticles. If the particle is oriented along a low index zone axis, the distribution of atoms on the surface can be imaged in profile, and the surface structure is directly seen with the full resolution power of a TEM.[41] This is a powerful technique for directly imaging the projected shapes of nanoparticles, particularly when the particle size is small. With consideration of the particle shape symmetry, HRTEM can be used to determine the 3D shape of small particles although the image is a 2D projection of a 3D object.[42]

The TEM results presented in this article were recorded either at 200 kV using a Hitachi HF-2000 TEM equipped with a field emission source or at 400 kV using a JEOL 4000EX HRTEM. The highly coherent source of the Hitachi TEM is suitable for imaging small clusters because of enhanced phase contrast, and a point-to-point image resolution of 0.23 nm can be achieved. In addition, this TEM is also equipped with energy dispersive X-ray spectroscopy and electron energy loss spectroscopy for chemical analysis. The JEOL 4000EX is an ideal machine for recording HRTEM images at a resolution of 0.17 nm.

Figure 2a shows a group of cubo-octahedral shapes as a function of the ratio, R, of the growth rate in the ⟨100⟩ direction to that in the ⟨111⟩ direction. The longest direction in a cube is the ⟨111⟩ diagonal, the longest direction in the octahedron is the ⟨100⟩ diagonal, and the longest direction in the cubo-octahedron ($R = 0.87$) is the ⟨110⟩ direction. The particles with $0.87 < R < 1.73$ have {100} and {111} facets, and are termed truncated octahedra (TO). The other group of particles has a fixed (111) base with exposed {111} and {100} facets (Fig. 2b). An increase in the area ratio of {111} to {100} results in the evolution of particle shapes from triangular pyramid to tetrahedron. TO particles have frequently been observed in Au, Pt, and Ag, while cubes and tetrahedra have been observed in Pt[43,44] and CoO.[36]

The small size of nanoparticles means that they usually contain no dislocations, but planar defects such as twins

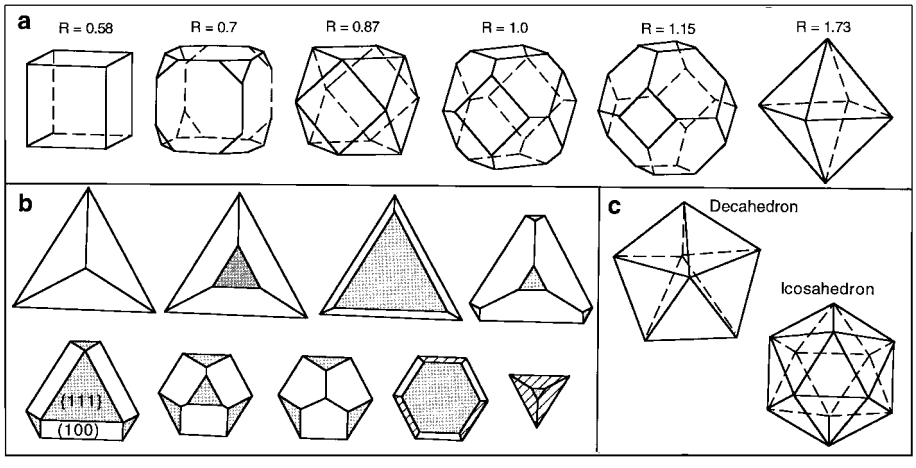

Fig. 2. a) Geometrical shapes of cubo-octahedral nanocrystals as a function of the ratio, R, of the growth rate along the ⟨100⟩ direction to that of the ⟨111⟩ direction. b) Shape evolution of a series of (111)-based nanoparticles as the ratio of {111} to {100} increases. The initial particle is bounded by three {100} facets and a (111) base, while the final one is a {111}-bounded tetrahedron. c) Geometrical shapes of multiply twinned decahedral and icosahedral particles.

  0935-9648/98/0101-0015 $ 17.50+.50/0

and stacking faults are abundant. The two most typical examples of multiply twinned particles (MTP) are decahedron and icosahedron.[45,46] Marks[42] has reviewed experimental studies on these types of particles and the surface energy for determining their shapes. HRTEM observations and the corresponding image simulation of the MTPs are described in detail by Buffat et al.[47] Starting from an *fcc* structured tetrahedron, a decahedron is assembled from five tetrahedra that share an edge (Fig. 2c). If the observation direction is along the five-fold axis and the conditions are ideal, each tetrahedron takes up an angle of 70.5°; five of them can only occupy a total of 352.6°, leaving a 7.4° gap. Therefore, strain must be induced in the particle to fill the gap.[48,49] An icosahedron is assembled using 20 tetrahedra that share an apex. Both types of MTPs have been observed in a variety of materials systems (and have been reviewed elsewhere[50]).

Figures 3a–c show the typical shapes of Au particles observed in the nanocrystals used to assemble NCSs. The shapes most frequently observed are TO and particles with a single twin. Decahedral particles are seen occasionally. A common feature of these particles is the {111} and {100} facets, which may strongly affect the crystal structure of the 3D assembly. For small particles, the number of atoms needed to form a specific particle shape is the so-called magic number, for example, the two TO Pt clusters with 79 and 225 atoms shown in Figure 3d.[51] Platinum can form cubic and tetrahedral shapes: the one indicated in Figure 3e is a small tetrahedron possibly with truncated corners.

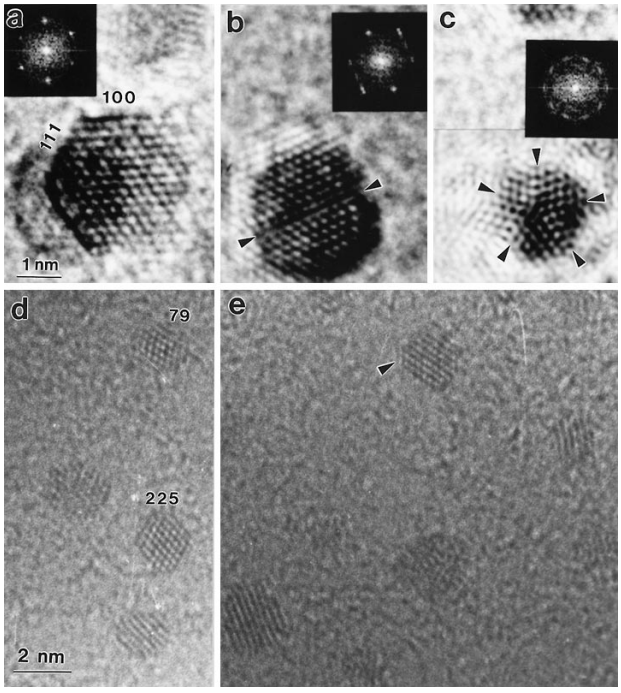

Fig. 3. a–c) Typical particle shapes observed in Au nanocrystals. d,e) Small-size truncated octahedral and tetrahedral clusters of Pt, where 79 and 225 indicate the likely number of atoms in the corresponding nanocrystals. (Pt particles were synthesized by Professor M. A. El-Sayed and Dr. T. S. Ahmadi.)

The shapes displayed by nanoparticles unambiguously illustrate that the assembly of nanocrystals is quite different from the packing of "hard" spheres, that is, the shapes, corners, and the distribution of thiolates on the surface are important. Therefore, the goal of the following sections is to illustrate approaches to the analysis of the self-assembled nanocrystal superlattice structures formed.

In addition to HRTEM, X-ray diffraction is a powerful tool for refining the structure of nanoclusters, particularly those smaller than 2 nm. If the particles are oriented randomly so that the entire assembly can be treated as a "polycrystalline" specimen composed of nanocrystals with identical structure but random orientation so that the scattering from each can be treated independently, the structure of the nanocrystals can be refined by quantitative comparison of the theoretically calculated diffraction spectra for different nanocrystal models with the experimentally observed ones. This was recently performed by Cleveland et al.[52,53] in the determination of decahedral Au nanocluster structures 1.7–1.9 nm in size.

4. 2D and 3D Assembly of Nanoparticles

As in the analysis of other materials, X-ray diffraction is the first choice for examining the formation of crystalline assemblies. The diffraction spectrum in the high-angle range is directly related to the atomic structure of the nanocrystal, while the spectrum in the small-angle region is directly associated to the ordered assembly of the nanocrystals.[8,28] By examining the diffraction peaks that are missing from the spectrum one may identify the crystallographic packing. This analysis is based on the assumption that each particle is identical in size, shape, and even orientation (i.e., the same X-ray scattering factor), so that the extinction rules derived from diffraction physics apply. In practice, however, a fluctuation in either the size, orientation, or shape can easily make this assumption untenable. This is the reason why a quantitative analysis of the low-angle diffraction spectrum is rather difficult. Therefore, caution must be exercised in interpretation of the 3D assembly using X-ray diffraction data. Nevertheless, X-ray diffraction is still the most powerful technique for evaluating the average interparticle distance D_{XRD}, and is a unique technique for studying the in-situ pressure- and/or temperature-induced phase transformations in nanocrystals.[27]

An alternative technique for studying nanocrystals is mass spectroscopy, which is a powerful technique for measuring the core size of nanoparticles. By measuring the mass distribution of the as-prepared nanoparticles, the particle size (or average diameter), D_{MS}, can be calculated if the density of the particle is assumed to be the same as in the bulk and the particle shape is approximated as spherical. Combined use of the data from X-ray diffraction and mass spectroscopy gives the difference $\Delta D = D_{XRD} - D_{MS}$, which can be compared with the length of the thiolate mol-

0935-9648/98/0101-0016 $ 17.50+.50/0

ADVANCED MATERIALS

ecule passivated on the particle to determine the depth of interpenetration (or overlap) between thiolate chains on forming the interdigitating molecular bonds. This type of study was illustrated to be an effective method for understanding the packing and interparticle interaction in Au systems.[25,54] In fact, an NCS is a structurally ordered nanocomposite of nanocrystals with organic molecules, and this material is an insulator if the chain molecule is long. By controlling the length of the thiolate, a transition from insulator to semiconductor or conductor can be introduced, resulting in tunable properties. This has been demonstrated for Ag NCSs.[81]

In addition, mass spectroscopy is also very powerful for the detection of the critical size of the smallest nanocluster that can be synthesized and the magic number of atoms comprising the cluster.[24] This type of analysis is unique to clusters in which the atoms have not formed a well-defined crystal lattice, prohibiting the use of X-ray diffraction and HRTEM.

Moreover, although X-ray diffraction may indicate ordered packing in the assembled nanocrystals, the range of ordering is still unknown. This is similar to the X-ray diffraction spectrum of a polycrystalline specimen, in which analysis of the grain size from the diffraction spectrum is rather difficult because there are many factors, such as defects, dislocations, and structural imperfections at surfaces/interfaces, that can give rise to line broadening. In this case, TEM is useful for imaging particle packing.

TEM specimens of NCSs are usually prepared under ambient conditions by depositing droplets of nanocrystal solution onto carbon films supported by Cu grids, only varying the drying time used when preparing the self-assembled nanocrystal superlattices. In all cases 3–5 μL of a concentrated solution of silver nanocrystals were applied to a TEM grid. Samples dried using no additional solvent took approximately 7–10 min until they appeared dry by eye. Analysis of this method showed that irregular crystals with little uniformity, symmetry, or crystal faceting were formed, although, on a smaller scale (tenths of micrometers), three-dimensional periodic nanocrystal packing was observed. As the samples were dried more and more slowly, via addition of toluene solvent during drying and covering with a watchglass, analysis showed increased uniformity in lateral size, shape, thickness, and crystal faceting.

A 2D monolayer of self-assembled Au particles is shown in Figure 4.[55] It is apparent that the particle size is uniform, but the ordered packing is only short range, as indicated by arrowheads. In the region where two layers overlap, the short-range order in each layer is overshadowed by the disordered component of the other layer. It appears that an ordered structure does not exist as the number of stacked layers is increased, but this is owing to complications from the 2D projection effect in TEM imaging. In this case, X-ray diffraction might show reasonably well-ordered structures. Therefore, one must realize the complications involved in TEM imaging compared to X-ray diffraction.

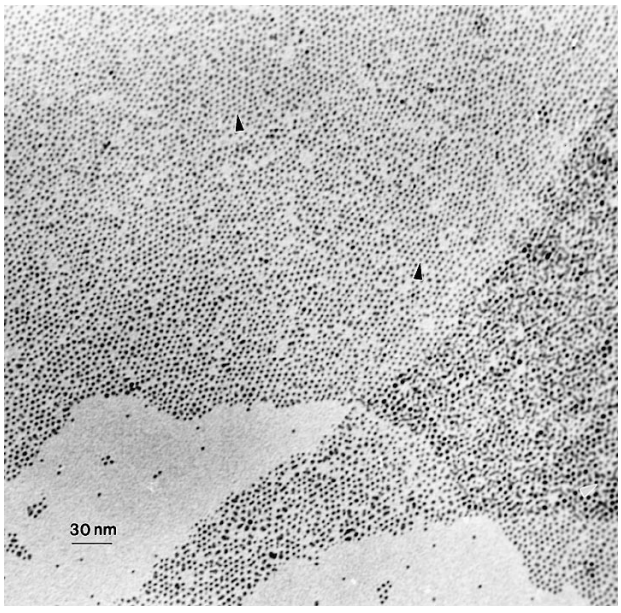

Fig. 4. TEM image of Au nanocrystals showing monolayer and double-layer self-assembly, where two regions with short-range order are indicated by arrowheads. The average particle size is 3–4 nm. (Nanocrystals were synthesized by Dr. S. Murthy.)

Judging from the TEM image shown in Figure 4 it might be concluded that the structure is rather disordered, but it may in fact still preserve some locally highly ordered structure. For multiply stacked layers, the ordered structure is apparent if the degree of order is high, such an example is given in Figure 5, where the stacking shows the $[011]_s$ projected symmetry of the face-centered cubic structure, and the subscript s represents the Miller index of NCSs. The angle measured from the lattice of the NCS is 71°, in excellent agreement with the theoretically expected value of 70.52° between the $(11\bar{1})_s$ and $(1\bar{1}1)_s$ planes. The structural model is based on other observations of the same specimen, as discussed later and shown in Figure 12.

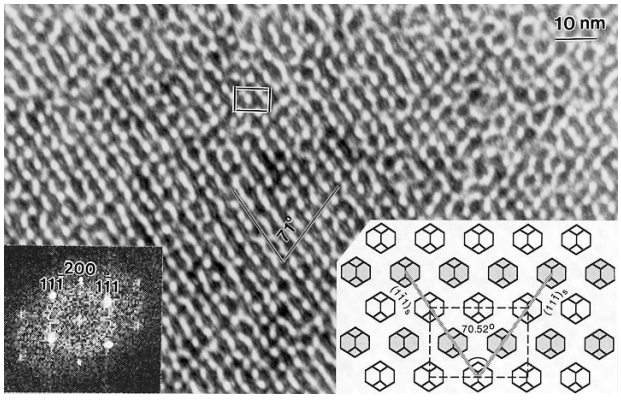

Fig. 5. $[011]_s$ TEM image of a 3D *fcc* assembled Au nanocrystal superlattice, where the projected unit cell is indicated and the structural model is shown in the inset, in which the particles located at an upper level with respect to the viewer are pasted in gray. A Fourier transform of the image is also shown and is indexed in the *fcc* system. The average particle size is 3–4 nm. (Nanocrystals were synthesized by Prof. R. L. Whetten.)

  0935-9648/98/0101-0017 $ 17.50+.50/0

5. Translational and Orientational Ordering

Translational ordering of NCSs can easily be seen via TEM images, but the analysis of orientational ordering of nanoparticles is a rather difficult task. Since the conventional bright-field TEM image is almost completely insensitive to the orientation of the nanoparticles, particularly when their size is less than a few nanometers (although HRTEM may be helpful for a small region), electron diffraction was used. A selected-area electron diffraction pattern recorded on a ~4 μm Ag NCS is shown in Figure 6.

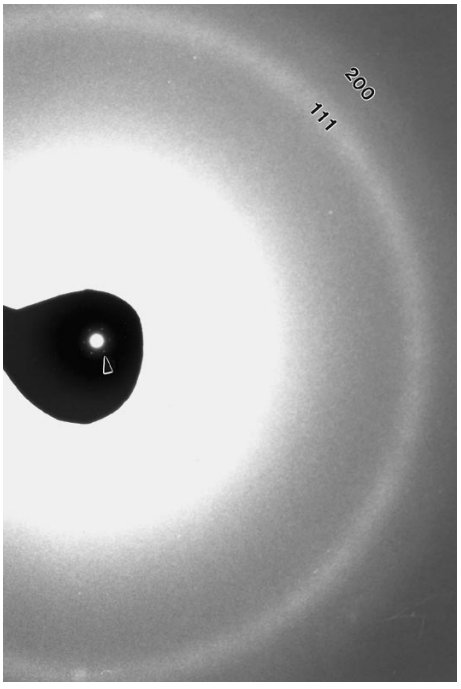

Fig. 6. An electron diffraction pattern recorded on an *hcp* packed Ag NCS, showing the 6-fold symmetry of the superlattice reflections at low angle, while the high-angle scattering from the atomic Ag lattices is a continuous ring pattern, indicating no average orientational order across a large specimen area (~4 μm).

The 6-fold symmetric diffraction pattern from the superlattice is apparent near the central transmitted spot, while diffraction from the atomic lattices of Ag gives a ring pattern, possibly indicating no orientational order in this region. Before reaching this conclusion one must, however, consider the short-range ordering characteristics in particle orientation. Dark-field TEM imaging can be useful for solving this problem.

Dark-field TEM images are formed using the electrons that are diffracted to angles away from the (000) central transmitted spot. By selecting the electrons falling in a specific angular range, one may find the real-space distribution of the particles that are oriented in a direction likely to give a Bragg reflection in the angular range selected by the small objective aperture for forming the image. Figure 7a is

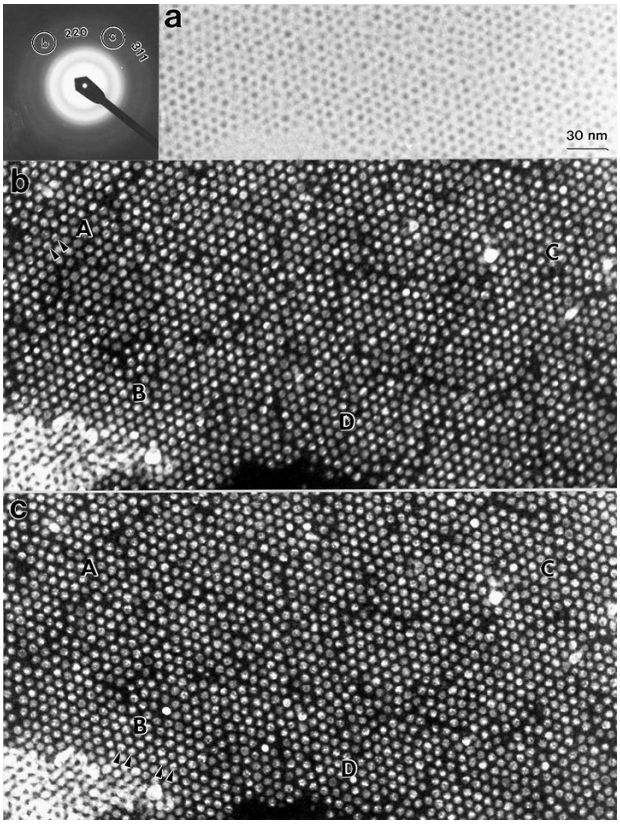

Fig. 7. a) Bright-field TEM image and the corresponding electron diffraction pattern of a self-assembled monolayer of Ag nanocrystals. b,c) Dark-field TEM images recorded in the same region by selecting the electrons scattered to the angular ranges indicated by the b and c circles in (a), respectively, showing the twinned structures of the particles and their short-range orientational order. The average particle size is 6 nm. (Nanocrystals were synthesized by Drs. I. Vezmar and M. M. Alvarez.)

a bright-field image of a monolayer Ag NCS and the corresponding electron diffraction pattern. To map the orientational distribution of the Ag particles, the reflection from the Ag atomic lattices, such as the (220) and (311) rings, is selected. Figures 7b and 7c are two dark-field images recorded by selecting the electrons scattered to the angular ranges indicated by circles b and c in the diffraction pattern, respectively; the size of the circle represents the approximate size of the objective aperture used. By examining the intensity distribution in the volume of each particle the astonishing fact was discovered that only part of the particle gives rise to the reflection selected by the objective aperture. This unambiguously proves that the particles are not single crystalline, but could have twin or multiple twin defects. By examining the intensity distribution across the entire image, it was found, based on the similarity in contrast of each particle, that the particles distributed in the regions indicated by A, B, C, and D have a common orientation. A few examples are indicated by arrowheads in the image. The short-range order in particle orientation is not seen in the electron diffraction pattern as it is an average of all the differently oriented particles.

0935-9648/98/0101-0018 $ 17.50+.50/0

ADVANCED MATERIALS

It is worth pointing out that the particles with circular contrast (see region D in Fig. 7c) may be multiply twinned. To confirm this, HRTEM images were recorded in the region (Fig. 8) in which singly twinned (T), single crystal (S), decahedral (D), and icosahedral (I) particles are observed; the majority of the particles contain twins, in agreement with the results from dark-field imaging. The twinned particles have more facets and appear to be close to spherical, thus their assembly is likely to be $(111)_s$ close-packed, as in the case of "hard" balls, in agreement with the electron diffraction pattern shown in Figure 6. It needs to be pointed out

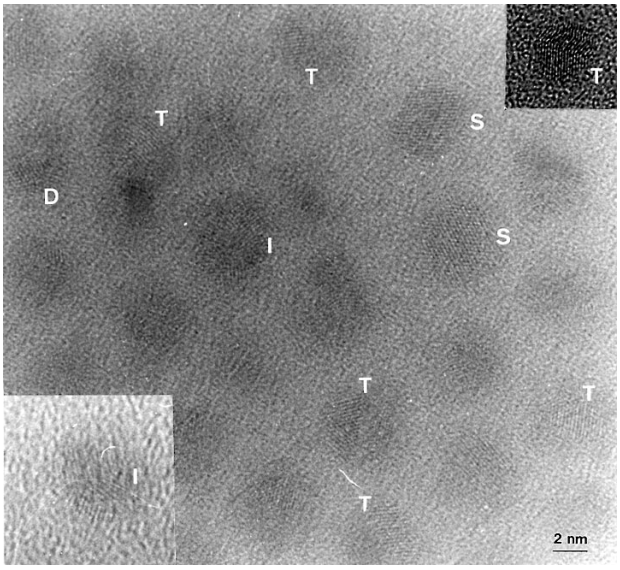

Fig. 8. HRTEM image of a self-assembled monolayer of Ag nanocrystals, showing the presence of single crystal (S), twinned (T), decahedral (D), and icosahedral (I) nanoparticles in a local region.

that the HRTEM image of the particles belonging to NCSs is rather difficult to record experimentally because of strong background noise from the carbon film and the thiolate passivating layer. This is a major obstacle prohibiting the application of HRTEM imaging to resolve the structure of NCSs, particularly when there are more than two stacked layers.

In NCSs a 6-fold projected symmetrical distribution of the particles is usually seen. This configuration could correspond to the *fcc* (or body-centered cubic, *bcc*) $[111]_s$ direction or the *hcp* $[0001]_s$ direction, provided no other type of packing is possible. To uniquely determine the 3D packing, 45° specimen tilting is required to change the imaging zone axis from $[111]_s$ (or $[0001]_s$) to another low index zone axis. This experiment is indispensable in order to pin down the answer.[16,19]

6. Nanocrystal Shape in 3D Assemblies

As demonstrated in Figure 3, nanocrystals can have shapes other than spherical, for example, TO. This is the case for Ag nanocrystals prepared by an aerosol technique.[21] We use this here as an example to illustrate the analysis of this type of structure. Figures 9a and b are two

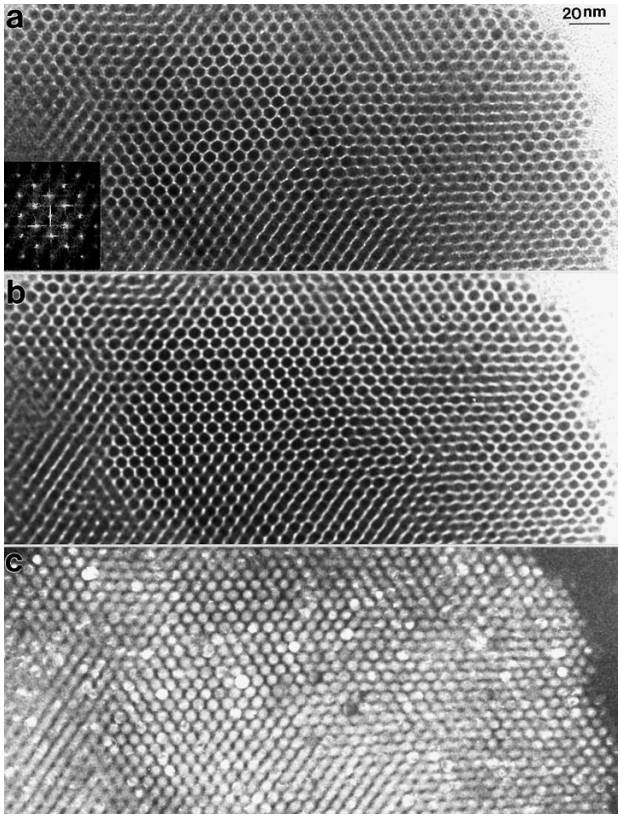

Fig. 9. a,b) Bright-field $[110]_s$ TEM images of a 3D *fcc* NCS assembled from faceted Ag nanocrystals, recorded under the conditions of in-focus and under-focus, respectively. The particle shapes are mainly dominated by truncated octahedra. A Fourier transform of the image is inset in (a). c) Dark-field TEM image recorded under the same condition as for Figure 8b, showing the single-crystal structure of the nanoparticles. The average particle size is 6–7 nm. (Nanocrystals were synthesized by Drs. R. L. Whetten and I. Vezmar.)

bright-field TEM images recorded on the same area of an NCS under two different defocus conditions. The image recorded under the near-in-focus condition (Fig. 9a) clearly illustrates the particle shapes, while the image recorded under the under-focus condition reveals the distribution of thiolate molecules on the surface of the particles, a point addressed later (Sec. 7). In the region with almost perfect particle packing, the shape of the nanocrystals is close to the [110] projection of a TO particle. From the geometrical configuration shown in Figure 2a, a TO particle is single crystalline with no twinning. Direct proof of this comes from dark-field imaging, as shown in Figure 9c, recorded on the same specimen region by selecting a portion of the (220) and (311) diffraction rings using a small objective aperture as used to record the images shown in Figure 7b. It is apparent that most of the particles show uniform bright contrast, indicating the absence of twins in the particle with reference to the image contrast shown earlier in

  0935-9648/98/0101-0019 $ 17.50+.50/0

Figures 7b and c. From the Fourier transform of the image (inset, Fig. 7a) the pattern is clearly the $[110]_s$ diffraction pattern of an *fcc* lattice.

The NCS was imaged from different perspectives to gather all the information needed to construct the 3D model. Figure 10a shows a $[111]_s$ image of the NCS, in which the 6-fold symmetry is clearly imaged. The $[110]_s$ image unambiguously shows the TO shape of the Ag nanocrystals as well as orientational ordering in the local region. Compared to the $[110]_s$ image shown in Figure 9a, the crystal shape is much more apparent in the image displayed in Figure 10b, although both images support *fcc* packing.

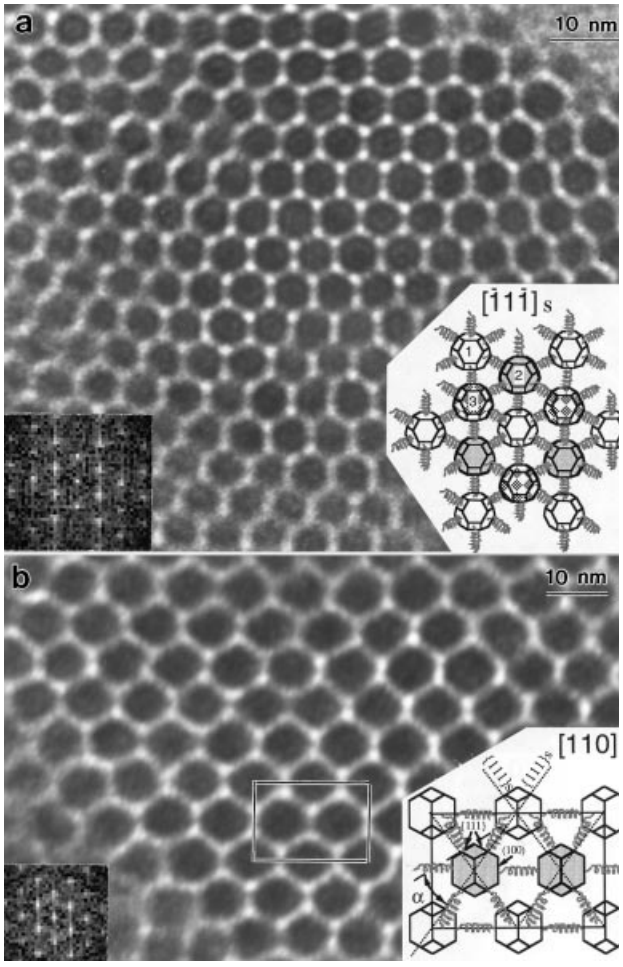

Fig. 10. $[\bar{1}1\bar{1}]_s$ (a) and $[110]_s$ (b) TEM images of a 3D *fcc* NCS assembled from TO Ag nanocrystals, in which the Fourier transform and the corresponding structural models are inset. The streaks in the patterns are due to the finite window used in the Fourier transform. The particles labeled 1, 2, and 3 and pasted with different patterns represent the first, second, and third layers of particles, respectively, counting from the substrate. The "springs" attached to the facets of the particles represent the bundled thiolate molecular bonds interconnecting the particles.

To confirm the *fcc* packing of the nanocrystals an image showing the $[110]_s$ and $[100]_s$ projections of the NCS is presented (Fig. 11a). The lattice constants measured from the A and B regions are consistent. More interestingly, it was noticed in region B, where the [100] image is shown, there is little difference in the contrast of the particle columns indicated by arrowheads, which possibly indicates that the number of the stacked particle layers is odd, for example, 3 or 5, so that the projected densities of the particles along the two adjacent columns are different by one. To refine the particle shape concluded from the low-resolution TEM image, HRTEM images were recorded using a large objective aperture that encloses a few Bragg beams, the results of which are given in Figure 11b, in which two TO particles are displayed and the boundaries of the nanocrystals are marked by solid lines. The {100} and {111} facets were clearly observed although some stacking faults were seen in the second particle. HRTEM images are the interference result of the electron waves diffracted by crystal lattices into different directions defined by the reciprocal lattice vectors, taking into consideration the characteristics of the objective lens for information transfer. Lattice fringes are usually observed in the image as a result of interference be-

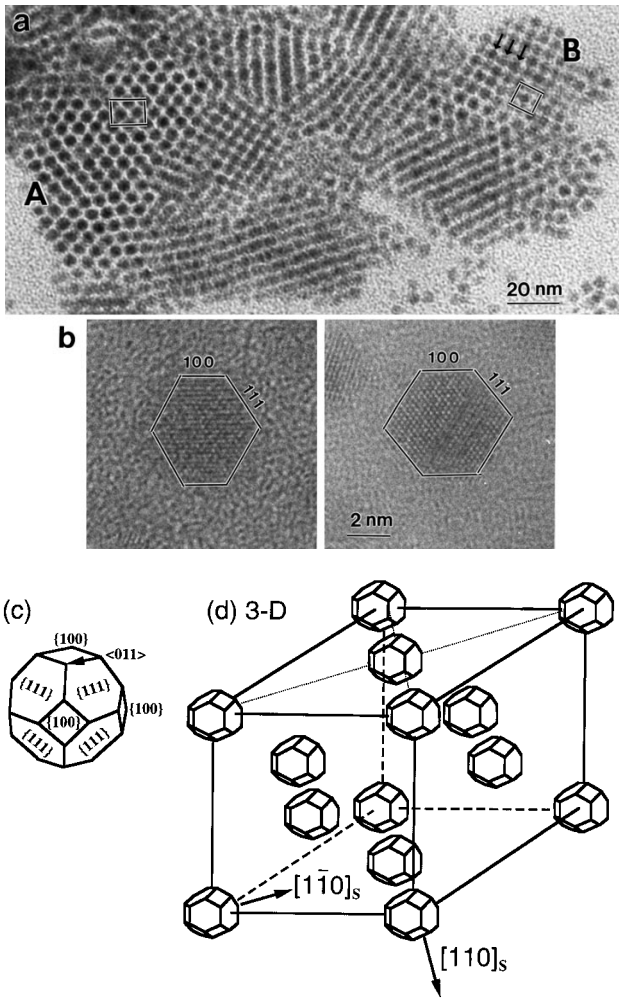

Fig. 11. a) TEM image of a 3D *fcc* Ag NCS showing the $[110]_s$ and $[100]_s$ projected symmetries of the crystal. b) HRTEM images of a monolayer NCS, showing the TO shape of the nanocrystals. c) A geometrical model of the TO particle shape. d) A structural model correlating the ordered particle orientation and the *fcc* packing of the superlattice based on the structural information provided in Figures 9–11 (a,b) [12].

0935-9648/98/0101-0020 $ 17.50+.50/0 *Adv. Mater.* **1998**, *10*, No. 1

ADVANCED MATERIALS

tween different Bragg beams, but the white or dark dots may or may not represent columns of the atoms, depending on the specimen thickness and lens defocus. Furthermore, fringes observed near nanocrystals may not correspond to any crystal lattice, such as the fringes observed at the upper-left side of the crystal shown in Figure 3b; such fringes are named "ghost" fringes as they result purely from electron interference rather than structure.[56] This phenomenon is quite often observed in HRTEM images recorded using a TEM equipped with a field emission source because of high coherence.

We now build a model that correlates the orientation of Ag nanocrystals with the lattice of the NCS. The majority of the Ag particles have the TO shape that is bounded by six {100} facets and eight {111} facets. When viewed along the [110] direction, two {100} facets and four {111} facets are projected edge-on (Fig. 11c). To summarize the data provided in Figures 9–11, the orientational relationship between the Ag particles and the nanocrystal lattice is [110] || $[110]_s$ and [002] || $[1\bar{1}0]_s$. A model is given in Figure 11d to illustrate the registered orientational relationship of the nanocrystals and the lattice of the NCS. The faceted structure of the Ag particles produces non-identical projected images when viewed along the $[110]_s$ and $[1\bar{1}0]_s$ directions, according to the proposed model. When the electron beam is parallel to the $[110]_s$ direction, the [110] orientation of the Ag particles is parallel to the $[110]_s$ direction of the superlattice, where four {111} and two {100} facets of the particle are parallel to the electron beam, in agreement with the image shown in Figure 10b. On the other hand, if the viewing direction is $[1\bar{1}0]_s$, the particle shape appears more like a sphere, such as the one displayed in region A in Figure 11a and the one shown in Figure 9. This exercise tells us that the particle shape should not be concluded from the information provided by a single image. It is highly recommended that the consistency of all the recorded images should be examined. Precisely said, the model proposed in Figure 11d is face-centered tetragonal in which $a_s = b_s \neq c_s$.

To examine the proposed model in detail, the $[110]_s$ projection of the model is inserted in Figure 10b, according to which an angle α is expected between the $(1\bar{1}1)$ facet (as indicated) of the Ag particle and the $(1\bar{1}1)_s$ plane of the superlattice, which is calculated to be 19.4° based on geometrical considerations. This angle was observed in the HRTEM image of an Ag NCS monolayer,[12] and the experimental result was 15.5° ± 2°, in reasonable agreement with the expected value, considering the distortion in the NCS lattice.

7. Bundling and Interdigitating of Interparticle Molecular Bonds

As I pointed out previously, the passivated thiolate molecules serve as the interparticle bonds for constructing the NCS. For particles whose shape can be approximated as spherical, the distribution of the thiolate chains on the surface is likely to be uniform without bundle formation. For faceted particles, however, the uniform passivation model may not be the case. It is also interesting to know if the thiolates are concentrated at the surfaces, corners, or edges. Here we use the information provided by TEM to show the bundling effect of the thiolate chains on the surfaces of nanocrystals. First I illustrate the physical mechanism used by HRTEM to provide this type of information.

For simplicity, we consider the electron phase modulation introduced by a crystal potential V. The kinetic energy (or momentum) is perturbed by the crystal potential, resulting in a small correction to the electron wavelength, which gives rise to phase modulation. Thus, the electron wavefunction after traversing a thin specimen is approximated by Equation 1,[57] where $\sigma = \pi/\lambda U_0$, λ is the electron wavelength in vacuum, U_0 is the acceleration voltage of the microscope, and V_p (see Eq. 2) is the projected potential of the crystal over the entire thickness d along the incident beam direction (e.g. the z-axis).

$$\Psi(x,y) \approx \exp[i\sigma V_p(x,y)] \tag{1}$$

$$V_p = \int_0^d dz\, V(\boldsymbol{r}) \tag{2}$$

This is known as the phase object approximation, and the contrast produced by this mechanism is called phase contrast. If the specimen is a weakly scattering object, so that $|\sigma V_p| \ll 1$, the wavefunction can be approximated as shown in Equation 3. This is the weak-phase object approximation, which representatively illustrates the physics involved in HRTEM, although it fails in most of the cases of interest.

$$\Psi(x,y) \approx 1 + i\sigma V_p(\boldsymbol{b}) - \frac{\sigma^2}{2}[V_p(\boldsymbol{b})]^2 \tag{3}$$

The electron wavefunction at the exit face of the crystal must be transferred through the lens system in TEM before reaching the recording plate. The effect introduced by the nonlinear information transfer characteristics of the lens is described by Abbe's imaging theory, according to which the intensity distribution in the image plane is can be described as in Equation 4,[41] where t_{obj} is the inverse Fourier transform of the objective lens transfer function $T_{obj}(\boldsymbol{u})A(\boldsymbol{u})$ in reciprocal space $\boldsymbol{u}$, $A(\boldsymbol{u})$ is the aperture function, and ⊗ indicates a convolution calculation.

$$I(x,y) = |\Psi(x,y) \otimes t_{obj}(x,y)|^2 \tag{4}$$

For imaging the shape of nanocrystals, the resolution of the TEM can be assumed to be much higher than the particle size so that one can take the spherical aberration coeffi-

  0935-9648/98/0101-0021 $ 17.50+.50/0

cient of the objective lens to be $C_s \approx 0$. Thus $T_{obj}(\boldsymbol{u}) \approx \exp(\pi i \Delta f \lambda u^2)$. The aperture function can be approximated by a narrow Gaussian function to represent the information transfer of the objective aperture, $A(\boldsymbol{u}) = \exp(-\pi b^2 u^2)$, where Δf is the defocus value and b is a parameter that characterizes the size of the objective aperture. Therefore, t_{obj} can be calculated accordingly (Eq. 5).

$$t_{obj} \approx \frac{1}{b^2 - i\Delta f\lambda} \exp\left[-\frac{\pi(x^2+y^2)}{b^2 - i\Delta f\lambda}\right] \quad (5)$$

Under the weak-phase object approximation, Equation 4 becomes Equation 6.

$$I(x,y) \approx 1 - 2\sigma V_p(x,y) \otimes \mathrm{Im}[t_{obj}(x,y)] + \sigma^2 |V_p(x,y) \otimes t_{obj}(x,y)|^2 - \sigma^2 [V_p(x,y)]^2 \otimes \mathrm{Re}[t_{obj}(x,y)] \quad (6)$$

This equation has two important results. The image contrast is directly related to the two-dimensional projected potential of the crystal. Thus, the image reflects the projected structure of the crystal. The other result is that the contrast of the atom rows is determined by the sign and real-space distribution of t_{obj}. We now examine the result of Equation 6 in two simple situations.

First the in-focus condition, $\Delta f = 0$, at which $\mathrm{Im}[t_{obj}(x,y)] = 0$ (Eq. 7).

$$I(x,y) = 1 + \sigma^2 |V_p(x,y) \otimes t_{obj}(x,y)|^2 - \sigma^2 [V_p(x,y)]^2 \otimes t_{obj}(x,y) \quad (7)$$

Since $t_{obj}(x,y)$ is a Gaussian-like function, the convolution of this with the projected potential is equivalent to rounding off the sharp corners of the object, i.e. reducing the resolution. However, the image contrast is directly related to the shape of the projected potential. This is the reason why images such as the one in Figure 9a give the shape of the nanocrystals. Since the projected potential of the passivating layer is much weaker than that of the core metal particle, the contrast produced by the thiolate is almost invisible because the contrast is related to $|V_p|^2$.

In the second case, where $\Delta f \neq 0$ but is small ($|\Delta f\lambda| \ll b^2$), the second and third terms in Equation 6 can be dropped because they are second-order effects (Eqs. 8a and b).

$$I(x,y) \approx 1 - 2\,\sigma V_p(x,y) \otimes \mathrm{Im}[t_{obj}(x,y)] \quad (8a)$$

$$\mathrm{Im}(t_{obj}) \approx \frac{\Delta f\lambda}{b^4}\left[1 - \frac{\pi(x^2+y^2)}{b^2}\right] \exp\left[-\frac{\pi(x^2+y^2)}{b^2}\right] \quad (8b)$$

$\mathrm{Im}(t_{obj})$ is a sharp decay function and its sign depends on the sign of Δf. This is the basis of contrast reversal with change of defocus. The image contrast is approximately scaled according to V_p, enhancing the influence of the thiolate layers. Thus the visibility of the thiolate layer is significantly increased compared to the case for $\Delta f = 0$, as shown experimentally in Figures 9b and 10.

Under the defocus condition of $\Delta f < 0$, $\mathrm{Im}(t_{obj}) < 0$, the regions with appreciable potential V_p shows darker contrast (note $V_p < 0$). This is the reason why the region with accumulated thiolate molecules shows darker contrast; the regions without any molecules or with lower molecule density show brighter contrast. Therefore, the distribution of bundled thiolate molecules is easily identified in Figures 9b and 10. Accordingly, the interparticle thiolate molecules can be schematically represented by springs, as shown in the models inset in Figure 10. Considering the symmetry of the image contrast, these springs have roots at the {100} and {111} facets rather than edges or corners. Thus the particles are packed as closely as possible into a face-to-face configuration. The non-uniform distribution of the thiolate molecules on the surface is the result of faceted particles. Images recorded at the defocus condition clearly show directional intermolecular bonds, with the *n*-alkylthiolate surfactant between the particles, for example, as in Figure 9, where the bright contrast dots are the open channels enclosed by bundled surfactant molecules. These bonds interconnect the facets of Ag particles, and they serve as the binding force that holds the particles together to form a 3D lattice. Recent TEM images formed by energy-selected electrons after ionization of the carbon K edge clearly indicate the bundled distribution of the thiolate on the nanocrystal surface, unambiguously proving this conclusion.[82] The interactions between the thiolate chains is via van der Waals forces with a bonding energy of ~0.1 eV. The bond length only reaches the first nearest neighbors.

From the structural point of view, these molecular bonds tend to align the facets on which they are connected in a parallel fashion, possibly resulting in a slight tilt/twist in the orientation of the particle. This is probably the reason why only one set of {111} fringes are often seen in the HRTEM image; a small tilt, even as small as 1°, destroys the visibility of the other set of {111} fringes, which are expected to appear in the image if the particles are oriented exactly with the [110] direction parallel to the incident beam.[12] The size of the open channels enclosed by the surfactant bonds was measured to be 1–2 nm, which could be useful for molecular filtering. Our experimental observations support the interdigitation model describing the interaction between the thiolate molecules belonging to two nanocrystals.[58]

We now return to Figure 10 to discuss the particle shape. Our experience has shown that $[111]_s$ TEM images are most frequency observed if the particle shape is fairly close to spherical. For particles with a TO shape, $[110]_s$ images are usually obtained.[12] This phenomenon may be associated to the interaction of the thiolate layer with the sub-

  0935-9648/98/0101-0022 $ 17.50+.50/0 *Adv. Mater.* **1998**, *10*, No. 1

ADVANCED MATERIALS

strate. The particle tends to have maximum contact with the substrate in order to lower the surface energy, indicating that the properties of the substrate could affect the crystallographic packing, but more research is needed to examine this problem. On the other hand, the $[111]_s$ image illustrated in Figure 10a may give a misleading interpretation of the particle shape. Based on the model displayed in Figure 11d, a $[\bar{1}1\bar{1}]_s$ projection of the model is shown in Figure 10a, in which the particle appears almost spherical in shape, although the 3D shape is TO. This result clearly warns us that the particle shape cannot be directly determined from the image recorded along the $[111]_s$ direction, while an image from the $[110]_s$ direction clearly shows the particle shape (Fig. 10b). Therefore, a specimen tilting experiment is indispensable to fully understand the shape of the particles. Experiments of this type usually require a tilt angle as large as 45°.

Scanning probe microscopy, which includes scanning tunneling microscopy (STM) and atomic force microscopy (AFM), is a powerful approach to directly imaging self-assembled organic monolayers. This study was carried out recently on alkanethiol self-assembly on Au(111) surfaces,[59,60] and the results support the bundling of thiolates on the surface of Au, in agreement with our conclusion from TEM.

8. Defect Structures in NCSs

It is well known that defects and dislocations are created in solid materials to accommodate local strain and deformation. Structural characterization of solid-state materials is usually concentrated on the analysis of defects and interfaces. Our task here is to illustrate the defect analysis in NCS using TEM, which cannot be provided by X-ray diffraction. A defect structure is a deviation from the ordered structure, and a full understanding of the periodic structure is the basis of analyzing defects.

8.1. "Cracks" and Point Defects

As pointed out earlier, the as-synthesized nanocrystals are dispersed in liquid, in which size selection according to mass is performed. NCSs are formed by depositing droplets of passivated nanocrystals on a solid-state substrate via a slow drying process. The diffusion of the nanocrystals on the substrate is possibly driven by hydraulic forces as drying takes place. Thus the wetting problem, the viscosity, and the limiting concentration of the nanocrystals determine the types of defects and their density. The TEM image shown in Figure 7b clearly illustrates the "microcracks" created in the packing of a monolayer of Ag nanocrystals, which are likely to be the result of wet-drying processes. Point defects are also frequently observed in NCSs.

8.2. Slip Planes

The slip is a typical microstructure of metallurgic materials and is an important structure, responsible, at least in part, for the deformation of materials. This type of structure is created by the sliding of part of the crystal parallel to the slip plane along a specific direction, namely the slip direction. This type of structure also occurs in NCSs.

Figure 12a shows a TEM image recorded on the same specimen used in Figure 5. The Au particles align along some lines, and the line directions form an angle of 107 ± 1°, exhibiting a "twin" relationship between the A, B, and C domains. To examine the registered orientational relationship between the particles and the lines, an HRTEM image of domain B was recorded and the results are given

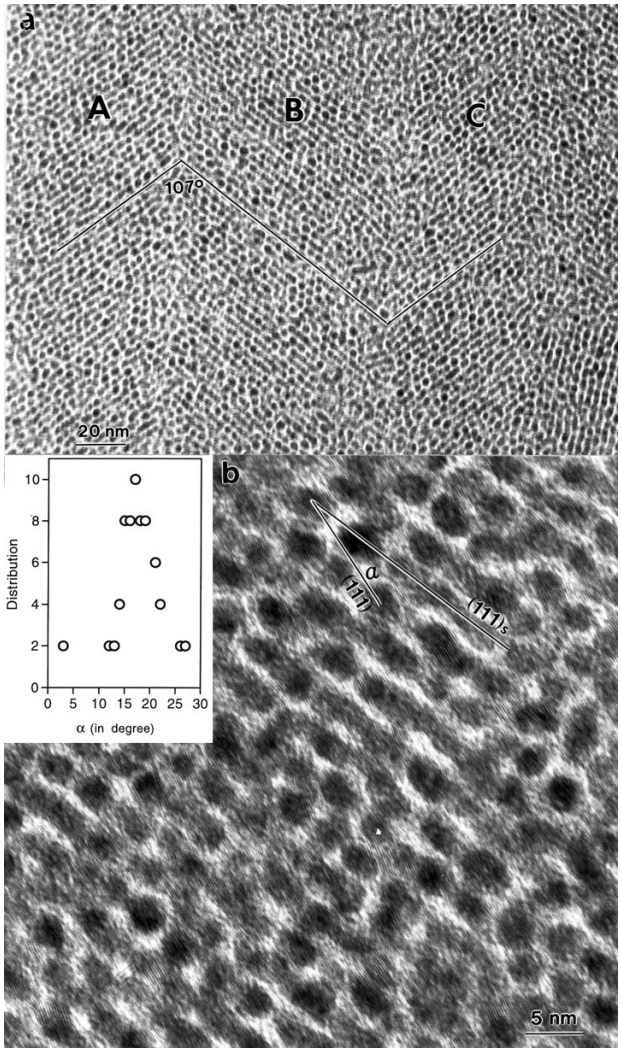

Fig. 12. a) TEM image of a self-assembled structure of Au nanocrystals, exhibiting "twin" symmetry. This structure was observed in the same specimen, the image of which is shown in Figure 5. b) An enlarged image of area B showing the single crystallinity of the gold particles and their ordered orientations with respect to the particle assembly plane. A statistical plot is given of the measured angles between the (111) plane of Ag and the $(111)_s$ plane of NCS. The particle shapes are likely to be dominated by TO, but the assembly could be affected by the size fluctuation of nanocrystals.

  0935-9648/98/0101-0023 $ 17.50+.50/0

in Figure 12b. The orientation of the Au {111} fringes can be measured with respect to the line direction (or the $(111)_s$ plane of the supercrystal). It is surprising that the average angle is $17 \pm 2°$ clockwise, as determined from the statistical plot inset in Figure 12b. More importantly, most of the particles are single crystals without twins, thus the crystal shape is possibly TO, according to the calculation of Whetten et al.[8] This image can be analyzed with reference to the *fcc* structural model provided in Figure 5.

The defect model is built starting from a perfect *fcc* structure oriented along the $[110]_s$ direction (Fig. 13a). If nanocrystal assembly is made layer by layer parallel to the substrate, the stacking positions of the nanocrystals can be shifted owing to the existence of four equivalent positions, marked A–D in the upper-left corner. It must be pointed out that these positions may not be allowed in conventional atomic packing because of short- and long-range interatomic interactions. In contrast, the packing of nanocrystals is primarily determined by the size of the interstitial positions compared to the available size of the nanocrystals. Among the four available positions, A and B or C and D can be taken up simultaneously by the next stacking layer, which is represented by layer 3 in the figure. The slip of layer 3 to occupy the A and B positions results in the formation of densely packed crystal rows, as shown at the right-hand side of the figure. If the particle shape is TO and the packing model can be described by a similar one to that shown in Figure 11d, the angle between the $(1\bar{1}\bar{1})$ planes of Ag and the $(1\bar{1}\bar{1})_s$ plane of the NCS is 19.4°, in agreement with the sign and magnitude of the angle measured in Fig-

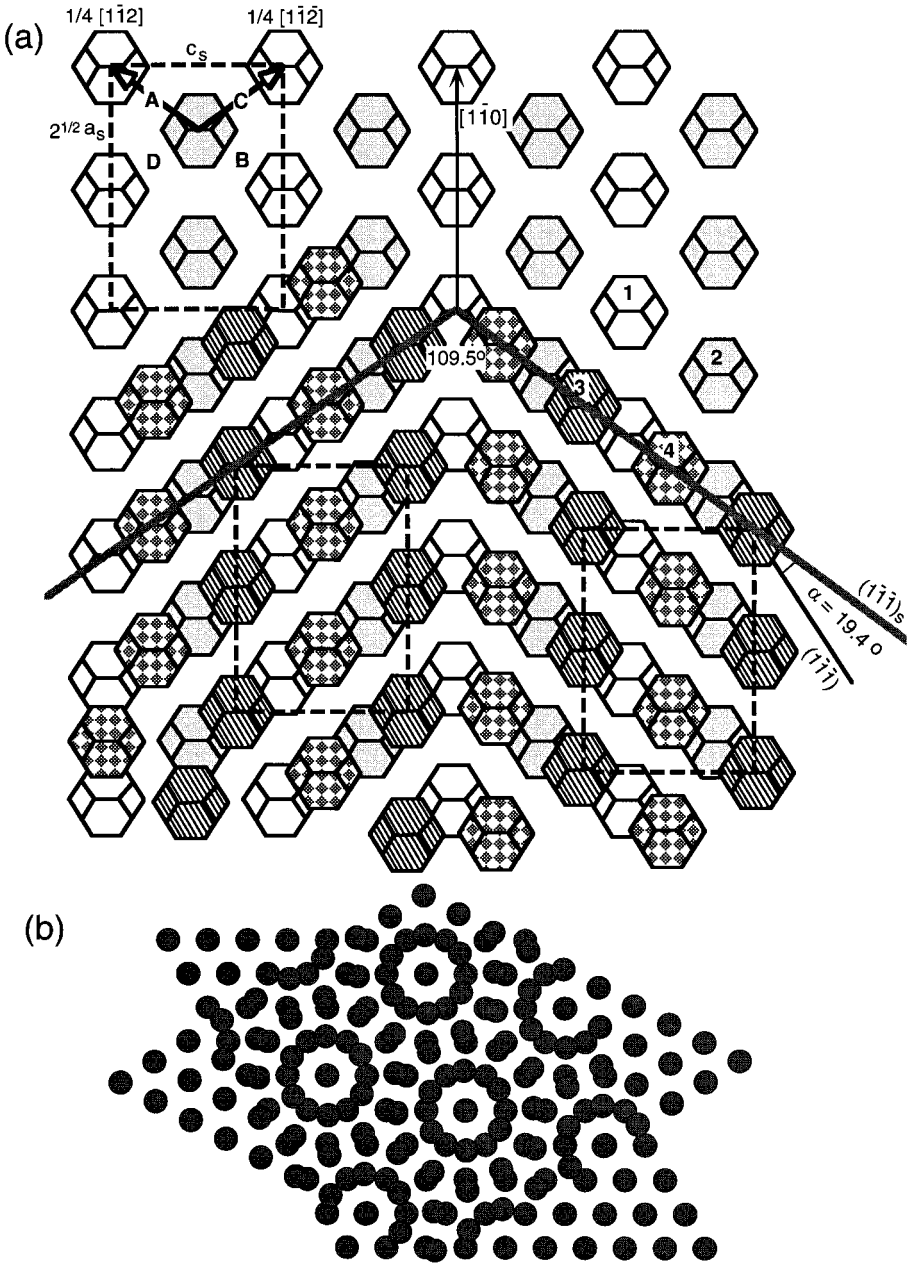

Fig. 13. a) A model of the twin structure observed in Figure 12, constructed by an *fcc* NCS oriented along $[110]_s$ with the introduction of a slip plane and different slip directions. The first two layers, labeled 1 and 2, preserve the *fcc* model, while the third and fourth layers are stacked on top with static displacements in the $(110)_s$ plane (see text). b) Formation of a Moiré pattern by stacking two (111) nanocrystal packed layers rotated 30° with respect to each other.

0935-9648/98/0101-0024 $ 17.50+.50/0 *Adv. Mater.* **1998**, *10,* No. 1

ADVANCED MATERIALS

ure 12b. The slip plane here is $(110)_s$ and the slip direction is $\frac{1}{8}[1\bar{1}2]$.

On the other hand, if the slip positions are C and D instead, the densely packed nanocrystal lines shown on the left-hand side of Figure 13a are formed. The two sets of lines on the left- and the right-hand side form a twin structure and the angle between the two is calculated theoretically to be 109.5°, in excellent agreement with the 107° measured experimentally. The slip plane here is $(110)_s$ and the slip direction is $\frac{1}{8}[1\overline{12}]$. The twin image is formed as a result of the two equivalent slip directions.

It is well known that the Moiré pattern presents itself in electron diffraction patterns, and it is generated by the stacking of two crystals oriented in different directions. Moiré patterns are also observed in NCSs, in which two assembled layers are stacked rotated at an angle to each other. For a $(111)_s$ packed layer stacked on the other layer rotated by 30°, a "donut" ring contrast is produced around the rotation center in the image (Fig. 13b). This was observed in Au NCSs.[61]

8.3. Twins and Stacking Faults

Twins and stacking faults are important microstructures in deformation of materials. These types of planar defects are also observed in NCSs, as shown in Figure 14. The presence of twin structures is directly observed in the Fourier transform of the image, exhibiting mirror symmetry. The twin and stacking planes are $(111)_s$, as indicated by arrowheads. The Ag nanocrystals have the TO shape and the NCS has *fcc* packing. The formation of these planar defects can be understood as follows.

As concluded from the discussion in Sections 6 and 7, intermolecular bonds are formed by the bundling of the surfactants on the {111} and {100} facets of the TO Ag particles. Thus the {111} facets can naturally interconnect with either the {111} facets or the {100} facets. The latter results in the rotation of the superlattice, leading to the formation of a $\{111\}_s$ twin. A model of this case is shown in the inset of Figure 14, in which a common layer shared by both sides of the twinned crystal is proposed, which serves as an intermediate step to rotating the particle orientations so that the face-to-face molecular bonding between particles still holds. By the same token, if the particle sites are shifted to modulate the interparticle distance, a stacking fault is formed. This modulation is limited to only one row of nanoparticles but still preserves the face-to-face packing.

Nanoparticle packing is a fascinating subject in which surprises occur. Figure 15a shows a 5-fold multiply twinned Ag nanocrystal assembly, which is similar to the projection of a decahedral particle (see Fig. 3c) along the 5-fold axis. Amazingly, by including 7 particles along each side of the "pentagon", a gap is created at the lower-left side, near to which a stacking fault is being created (see the arrowhead). As discussed earlier, strain must be present in the decahedral particle to fill the gap on the atomic scale. This rule also applies to NCSs although the Ag nanoparticles are TO in shape and are *fcc* packed. A corresponding structural model of the multiply twinned NCS is given in Figure 15b, where the particles are packed following the face-to-face rule. This model is proposed for a 2D projected multiply

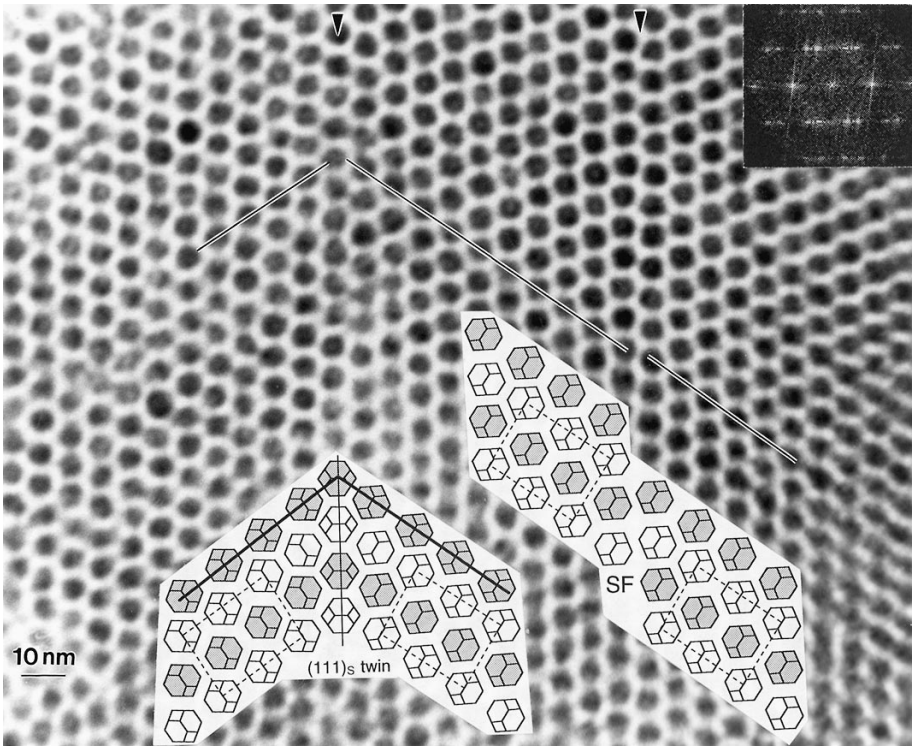

Fig. 14. TEM image of an *fcc* Ag NCS with twin and stacking fault planar defects, where the models for the twin and stacking fault defects are given. The average particle size is 6 nm.

  0935-9648/98/0101-0025 $ 17.50+.50/0

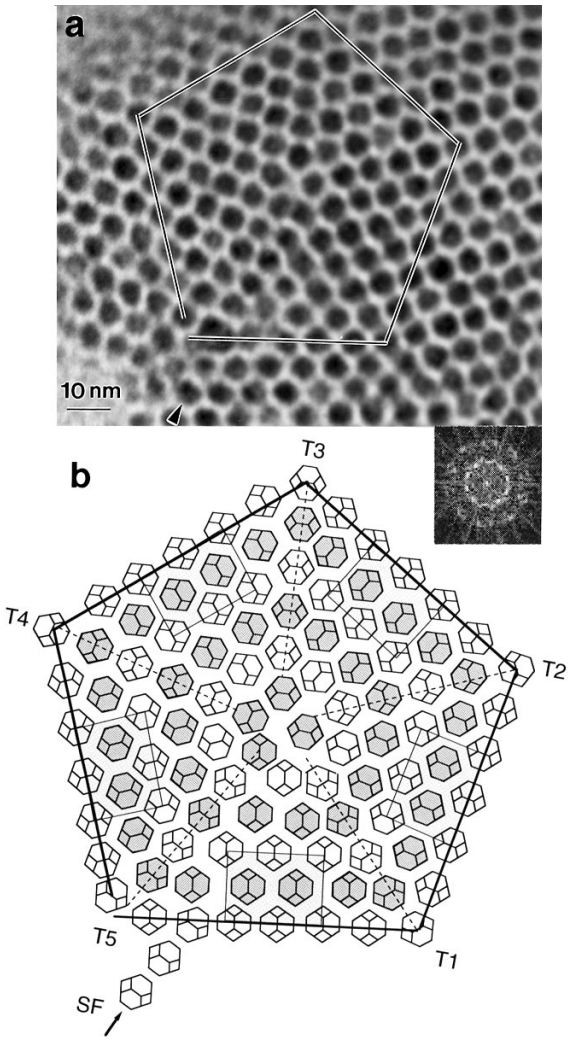

Fig. 15. TEM image of an *fcc* self-assembled Ag nanocrystal array showing a 5-fold multiply twinned structure. The inset is a Fourier transform of the image. b) A structural model of the Ag nanocrystal aggregate comprised of faceted TO particles, where a stacking fault is being formed at the low-left corner. (The TEM image was recorded by Dr. S. A. Harfenist.)

twinned NCS without consideration of the thickness variation across the assembly for a 3D decahedral NCS. From the image contrast, this nanocrystal assembly is likely to be a thin, platelet nanocrystal.

The atomic-scale decahedral particle model was first proposed by Ino[45] with reference to TEM micrographs, and a detailed crystallographic study of the multiply twinned particles has been given by Yang.[62] To understand the formation and stability of the decahedral particle, Ino[63] calculated the total free energy for different types of particles within the framework of the uniform strain model, assuming bulk values for the cohesive, surface, twin boundary, and elastic strain energies and for the adhesive energy to the surface. Mainly owing to the balance between energy gained by having low-surface-energy, external facets and energy spent in creating twin boundaries and also due to the increasing influence of elastic strain energy with size, he found that below a certain critical size the icosahedral particle is the most stable, while the decahedral particle is quasi-stable. In fact, both decahedral and icosahedral particles have been observed. With reference to the observation of the 5-fold twinned NCS, it would be interesting to calculate the energy associated with this packing and its stability, but the interface and surface energies may be unknown.

In addition to the planar defects, edge dislocation and pairs of edge dislocations have been observed in Ag NCSs.[17] Similar to conventional materials, strain is also present in NCS materials except the magnitude of strain could be much lower.

8.4. Distorted Structures

The assembly of nanocrystals is greatly complicated by their shape and, in some cases, the unit cell of the superlattice is distorted so much that the crystal structure cannot easily be assigned. Figure 16 shows two TEM images of the same specimen region of an Ag NCS recorded under

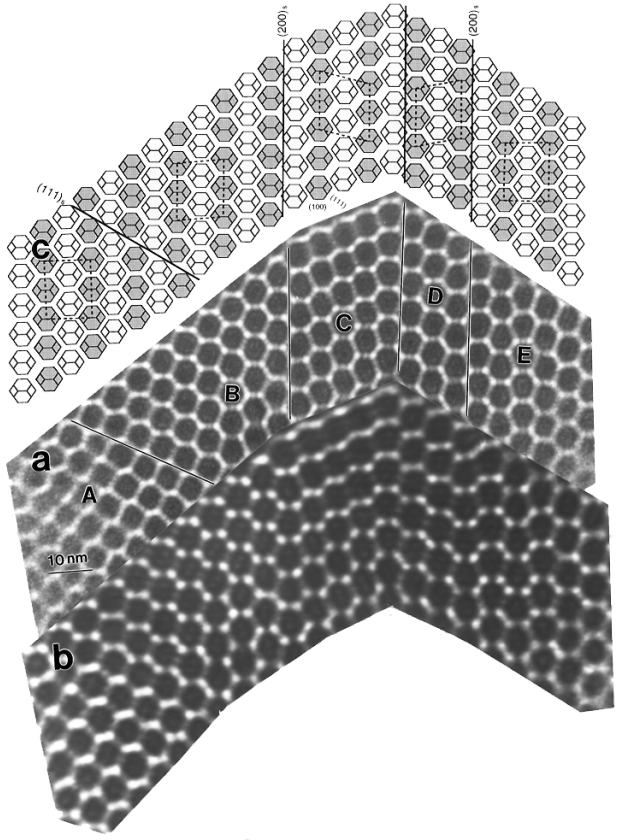

Fig. 16. a,b) $[110]_s$ TEM images of a 3D "*fcc*" NCS assembled from TO Ag nanocrystals, recorded under the conditions of in-focus and under-focus, respectively. The particle shape is clearly seen in the in-focus image, and the defocused image strongly enhances the visibility of the bundled molecular bonds on the particle surface, where the white dots are the open channels enclosed by the bundled thiolates. (The TEM image was recorded by Dr. S. A. Harfenist.) c) A structural model of the observed distortion in the nanocrystal array.

0935-9648/98/0101-0026 $ 17.50+.50/0 *Adv. Mater.* **1998**, *10*, No. 1

ADVANCED MATERIALS

slightly different defocus. The in-focus image clearly shows the TO shape of the Ag nanocrystals (Fig. 16a), while the bundling of the surfactant is more obvious in the defocused image (Fig. 16b). The assembly of nanocrystals here can be divided into five regions, A–E; the boundaries between them are indicated by solid lines. By tracing the shape of the particles located at each site, a model is built (Fig. 16c) in which the unit cells are indicated with dashed lines. The model is based on the orientation of the Ag nanocrystals as determined from the defocused image with reference to the distribution of open channels. It is striking that the shape of the unit cell is greatly distorted from region to region and in some areas, such as C and D, the unit cells hardly match the $[110]_s$ projection of *fcc* packing. In contrast, the $(200)_s$ plane of the NCS is preserved in each domain, while the orientation of the $\{111\}_s$ planes is distorted.

Finally, a "woodpecker" pattern, assembled by a monolayer of 6 nm Ag nanocrystals, is shown in Figure 17. The 2D unit cell is indicated by a rectangle, and three possible models are shown as the particle shape and orientation are unclear in the image. Model A was built based on the 3D *fcc* model provided in Figure 11c, in which the longer side of the particle is perpendicular to the longer side of the unit cell, but this is inconsistent with the observations. Model B is based on Model A except the geometrical shape of the Ag particles is adjusted to increase the area of the (100) facets, so that the model fits the observed dimensions. Alternatively, the orientation of the Ag particle could be rotated 90° to match the longer side of the particles with respect to the unit cell, as shown in Model C. Both Models A and B preserve the rule of face-to-face packing, while Model C is corner-to-corner. From our experience of analyzing NCSs of Ag particles Model C is unlikely.[12] Therefore, Model B is the most reasonable choice.

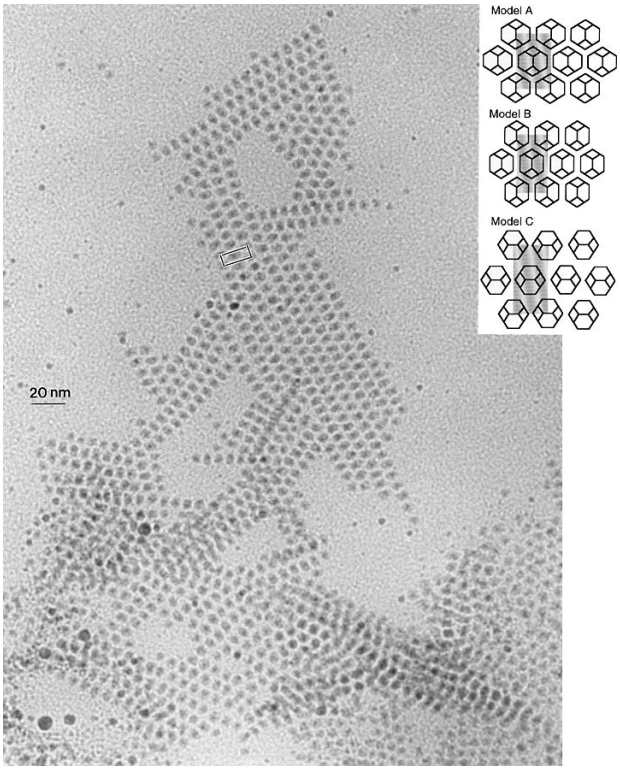

Fig. 17. TEM image of a "woodpecker" assembled from a monolayer of Ag nanocrystals with sizes 6–8 nm. The three possible structural models are also shown, but only Model B appears likely.

9. Dynamic Diffraction in NCS Imaging

It is well known that electron diffraction is dominated by dynamic scattering, leading to the extensive development of multiple scattering theory for electron diffraction.[64] For specimens thicker than 2–3 nm, dynamic diffraction theory is required for quantitative data analysis. In NCS analysis, dynamic scattering is also inevitable although the number of stacked layers is low. Figure 18a shows a bright-field

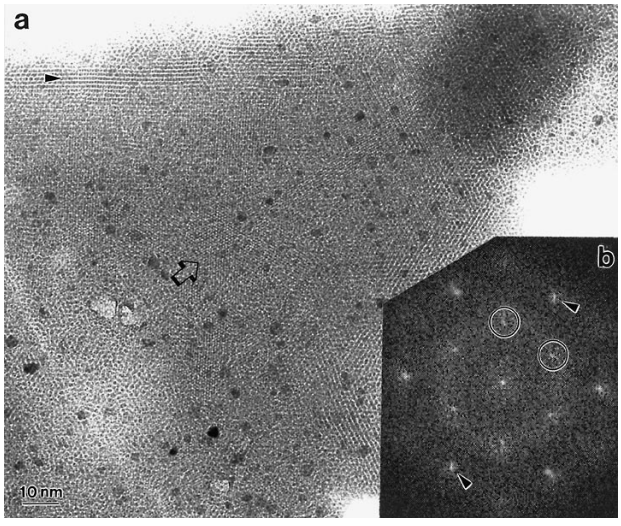

Fig. 18. a) TEM image of a superlattice structure assembled from multilayers of Ag nanocrystals, where the real particle sizes are seen at the thin-edge region and lattice fringes produced by many-beam interferences are visible in the middle. b) A Fourier transform of the image showing higher order Bragg reflections from the NCS.

TEM image of an Ag NCS. The particle size is seen at the edge of the specimen where the number of stacked layers is likely to be one or two. However, in the region with multilayer stacking, fringes considerably smaller than the interparticle distance are observed. A Fourier transform of this image is given in Figure 18b, which reveals the presence of the second-order diffraction spots from the NCS. The interference of these beams with the central transmitted beam or the beams located at the opposite side in the pattern could give rise to fringes with spacings of $a_s/(h^2 + k^2 + l^2)^{1/2}$ and/or $a_s/[2(h^2 + k^2 + l^2)^{1/2}]$ (for cubic structures) in the image, where $(hkl)_s$ are the Miller indices of the reflection. This is purely a dynamic many-beam interference effect, as in conventional HRTEM.

Image simulation using the proper dynamic scattering theory is required if one is interested in quantitative anal-

  0935-9648/98/0101-0027 $ 17.50+.50/0

ysis of the contrast. The calculation is performed by constructing a super unit cell in which a nanocrystal is considered as an "atom" placed at a lattice site. This type of calculation was performed by Bentzon and Thölén[38] to refine the crystal structure of the 3D NCS, with which the image of *fcc* $[111]_s$ can be distinguished from that of *hcp* $[0001]_s$ based on the difference in stacking sequences, particularly when the number of stacked layers is an odd number. The calculation is essential to interpretation of the "triangle" shape contrast observed in the TEM image.[16]

STM and AFM can be used to measure the thickness of the stacked layers,[16] and the general thickness is limited to no more than 20 layers. Dynamic calculations are currently being carried out to match the contrast observed in TEM images of the faceted Ag NCS taken in the defocus condition, such as the one shown in Figure 16b, to refine the density of bundled thiolate molecules on the nanocrystal surface.[65]

10. Growth Mechanism

Although NCSs have been grown for several different types of materials, the growth mechanism is still an open question. In most of the TEM observations, it is seen that the nanocrystals uniformly adhere to the substrate surface with no "piling up" among pieces of NCS, suggesting that the NCSs are formed on the liquid surface during the slow drying process. For TEM observation, a droplet of diluted solution is deposited on a carbon film; a slow drying process is critical for forming large size, ordered NCSs. Nanocrystals are believed to be uniformly suspended in the solution at first. If the diffusion speed of the nanoparticles in the liquid is slower than the evaporation speed of the liquid surface, the particle concentration is expected to increase locally immediately beneath the liquid surface, possibly resulting in the self-assembly of a 2D monolayer at the liquid surface; the surface tension might be the force that attaches the assembly to the liquid surface. As the evaporation continues, a second layer can be formed on top of the first layer if there are enough particles in the solution. Finally, when the evaporation reaches the substrate, the 2D assembled NCS layer(s) may be broken due to the unmatched curvature between the liquid droplet and the flat substrate surface, but no overlap between the large size NCSs would be possible.

From a structural point of view, most of the NCSs comprised of spherical nanoparticles have been found to have a platelet structure and are large size monolayers,[16] indicating the growth is a layer-by-layer "epitaxial" growth. This growth is possible if the nanocrystals are driven to diffuse towards the liquid surface. This is evident on examining the crystallinity of Ag NCSs grown by a slow, dilute drying process.[16] Moreover, for faceted nanocrystals, the self-assembled NCSs frequently show platelet structures and, more importantly, planar defects such as twins and stacking faults are usually observed, indicating that each layer is grown row by row and particle by particle, in support of the diffusion model. From the experimental observations of Harfenist et al.,[16] the triangular platelet structure of Ag NCSs is bounded by three {110} facets and the plate normal is $[111]_s$. This type of structure is likely to be grown from a single nucleation site followed by a row-to-row 2D growth along ⟨110⟩, forming a triangular monolayer. A continuous layer-by-layer epitaxial growth on top of this triangular layer as the particles are provided may form the platelet structure. The smooth morphological structure of NCSs indicates that particle diffusion is much faster than the rate of arrival of the particles, and the "hit-and-stick" model is not appropriate.[66] This growth mechanism is proposed based on the current limited experimental data. More observations are required to examine this model in detail.

11. Discussion and Prospects

For future applications, large size NCSs must be grown so that a variety of electronic and mechanical properties can be measured. A new precipitation technique is needed to expedite the growth of large size NCSs. NCSs examined by TEM have mostly been grown on carbon films. The effect of the supporting film on the packing is unclear. It would be interesting to examine the packing of NCSs if the same type of nanocrystal is deposited on alternative substrates, such as graphite, NaCl, mica, or MoS_2. On the other hand, the presence of the supporting film greatly affects the quality of HRTEM images because of the strong effect of the amorphous layer, particularly at high magnification. Image simulation indicates that such an effect can totally suppress the contrast from the particle at specific defocus conditions.[67]

As pointed out earlier, the bond strength of the thiolate molecule is in the order of 0.1 eV. This is rather weak for a single molecular chain. As observed by TEM, the thiolate molecules tend to be bundled on the surface, so that the interparticle bond strength is the sum of the strengths of all the chain molecules, which can be significant. In fact, TEM observations using 400 keV TEM at room temperature do not result in significant structural damage even after illumination for as long as 30 min, simply illustrating the high strength produced by integrated molecular bonding.

In-situ experiments on NCSs are important for studying the structural stability and phase transformation behavior. The results can be compared to those predicted by the molecular dynamic calculations of Luedtke and Landman.[58] Figure 19 shows a comparison of the monolayer assembled nanocrystal arrays of CoO when the specimen was annealed in situ from room temperature to 600 °C, during which the thiolates evaporated/decomposed and the CoO nanocrystals reacted with the residual carbon and formed Co_2C and Co_3C nanocrystals. The monolayer structure is maintained, possibly due to adhesion to the carbon support and, in contrast, the areas of multilayer nanocrystal assem-

0935-9648/98/0101-0028 $ 17.50+.50/0 *Adv. Mater.* **1998**, *10*, No. 1

ADVANCED MATERIALS

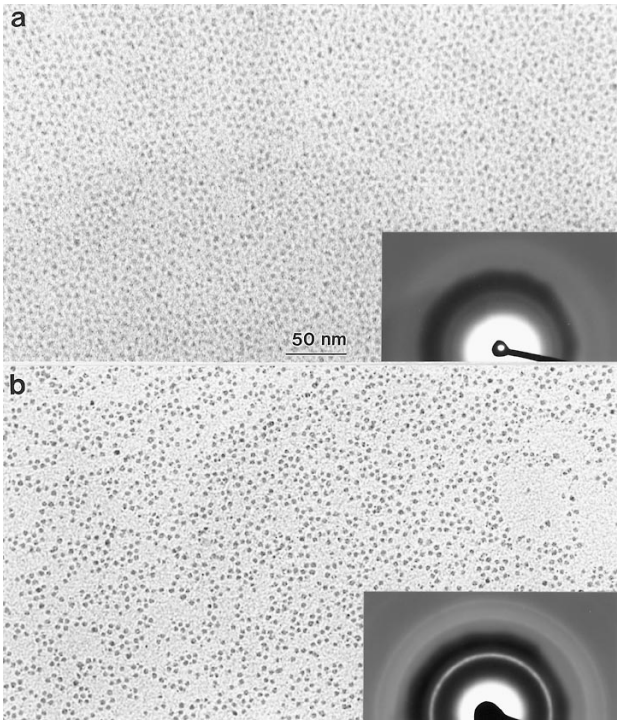

Fig. 19. A comparison of monolayer nanocrystal arrays of tetrahedral CoO before (a) and after (b) in-situ annealing in the TEM from room temperature to 600 °C, showing the formation of Co_2C and Co_3C produced by a replacement reaction at higher temperatures. The structural transformation is clearly evident in the diffraction patterns, as shown in the insets. The shape of the particles changes from tetrahedral to cubic-like.

bly formed larger Co_2C particles.[68] Nevertheless, this experiment proves the strong influence of the substrate on the structural stability of NCSs. The degradation of Ag_2S NCSs in air was reported by Motte et al.,[19] but the structure of Ag NCSs and Au NCSs studied by me and my coworkers were found to be stable in air even six months after preparation.

Electron holographic imaging and energy-filtered TEM imaging are two new emerging techniques associated with TEM. Both techniques can be very useful for studying NCSs. Electron holography is an imaging process based on the interference properties of electron waves that permits both the amplitude and phase of the object wave (i.e., the "true" image of the object) to be recovered.[69,70] By mapping the phase distribution of the electron wave, this technique can be useful to determine the 3D shape of the nanocrystals[71] and the surface distribution of the passivated thiolate layers on the nanocrystal surface, provided the substrate effect can be eliminated. It is recommended that HRTEM and electron holography are applied complimentarily to determine the particle shape.

Electron holography can also be applied to map the magnetic moment of magnetic particles. For magnetic materials, the phase of the electron wave is modulated by the magnetic field of the specimen owing to the Aharonov–Bohm effect.[72] Quantitative measurement of this phase via electron holography permits precise determination of the local magnetization. Thus, the magnetic field of the domains can be accurately determined. This analysis is possible if a magnetic-field-free specimen environment is created in TEM. This is possible with the use of a Lorentz lens. It has been successfully demonstrated that this type of analysis is feasible for magnetic particles as small as 10 nm[73] and larger ones as well.[74]

Energy-filtered electron imaging is performed with the use of an electron energy loss spectroscopy system on a TEM by selecting the electrons that have lost a specific energy, corresponding to the characteristic ionization edge of an element, such as the carbon K edge.[75] This type of image, after proper subtraction of background using the images acquired in the pre-edge regions, gives, for example, a distribution map of the thickness projected carbon density. This type of analysis could provide new insight into the distribution of thiolate molecules on the surface of nanocrystals, possibly leading to a new understanding of interparticle molecular bonding and the bundling effect of the chain molecules. This has been demonstrated recently in studies of Ag NCSs.[81,82]

In this article we concentrated mainly on the image analysis of nanoparticles with simple structures. For nanoparticles containing transition/rare-earth elements, the valence states of the metal cations can be determined at a spatial resolution better than 20 nm, using the white line intensities observed in the spectra of electron energy loss spectroscopy with reference to the spectra acquired from standard bulk specimens.[76–79] This technique has had dramatic success in refining the structures of CoO nanocrystals[36] and Fe_2O_3 and Mn_2O_3.[80]

In conclusion, it can be claimed that nanocrystal engineered superlattices are a new type of materials, different from either a single particle or the bulk materials. This is an open field and many exciting phenomena remain to be discovered. Materials of this type could have significant impact on future electronics, optics, and magnetic storage devices. It is anticipated that this review will serve as a basic guide to structure analysis of NCSs using transmission electron microscopy and associated techniques.

Received: June 2, 1997

[1] D. J. Wales, *Science* **1996**, *271*, 925. All the review articles in the February 16 issue of *Science*, **1996**.
[2] M. A. Kastner, *Phys. Today* **1993**, *46(1)*, 24.
[3] L. Brus, *Appl. Phys. A* **1991**, *53*, 465. A. P. Alivisatos, *Science* **1996**, *271*, 933.
[4] L. N. Lewis, *Chem. Rev.* **1993**, *93*, 2693.
[5] R. Freer, *Nanoceramics*, Institute of Materials, London **1993**.
[6] D. D. Awschalom, D. P. DiVincenzo, *Phys. Today* **1995**, *48(4)*, 43. J. Shi, S. Gider, K. Babcock, D. D. Awschalom, *Science* **1996**, *271*, 937.
[7] J. F. Smyth, *Science* **1992**, *258*, 414.
[8] R. L. Whetten, J. T. Khoury, M. M. Alvarez, S. Murthy, I. Vezmar, Z. L. Wang, C. C. Cleveland, W. D. Luedtke, U. Landman, *Adv. Mater.* **1996**, *8*, 428.
[9] P. V. Braun, P. Osenar, S. I. Stupp, *Nature* **1996**, *380*, 325.
[10] H. Weller, *Angew. Chem. Int. Ed. Engl.* **1996**, *35*, 1079.
[11] R. L. Whetten, J. T. Khoury, M. M. Alvarez, S. Murthy, I. Vezmar, Z. L. Wang, C. C. Cleveland, W. D.Luedtke, U. Landman, in *Chemical Physics of Fullerenes 5 and 10 Years Later* (Ed: W. Andreoni), Kluwer, Dordrecht, The Netherlands **1996**, p. 475.

  0935-9648/98/0101-0029 $ 17.50+.50/0

[12] S. A. Harfenist, Z. L. Wang, M. M. Alvarez, I. Vezmar, R. L. Whetten, *J. Phys. Chem.* 1996, *100*, 13 904.
[13] R. G. Nuzzo, D. L. Allara, *J. Am. Chem. Soc.* **1983**, *105*, 4481.
[14] J. Dorogi, J. Gomez, R. Osifchin, R. P. Andres, R. Refenberger, *Phys. Rev. B* **1995**, *52*, 9071.
[15] D. V. Leff, P. C. Ohara, J. R. Heath, W. M. Gelbart, *J. Phys. Chem.* **1995**, *99*, 7036.
[16] S. A. Harfenist, Z. L. Wang, M. M. Alvarez, I. Vezmar, R. L. Whetten, *Adv. Mater.* **1997**, *9*, 817.
[17] J. R. Heath, C. M. Knobler, D. V. Leff, *J. Phys. Chem. B* **1997**, *101*, 189.
[18] L. Motte, F. Billoudet, E. Lacaze, M.-P. Pileni, *Adv. Mater.* **1996**, *8*, 1018.
[19] L. Motte, F. Billoudet, E. Lacaze, J. Douin, M.-P. Pileni, *J. Phys. Chem. B* **1997**, *101*, 138.
[20] J. H. Fendler, F. C. Meldrum, *Adv. Mater*. **1995**, *7*, 607.
[21] M. M. Alvarez, I. Vezmar, R. L. Whetten, *J. Aerosol Sci.*, in press.
[22] M. Brust, M. Walker, D. Bethell, D. J. Schiffrin, R. Whyman, *J. Chem. Soc., Chem. Commun.* **1994**, 801.
[23] M. Brust, J. Fink, D. Bethell, D. J. Schiffrin, C. Kiely, *J. Chem. Soc., Chem. Commun.* **1995**, 1655.
[24] M. M. Alvarez, J. T. Khoury, T. G. Schaaff, M. Shafigullin, I. Vezmar, R. L. Whetten, *Chem. Phys. Lett.* **1997**, *266*, 91.
[25] M. Shafigullin, M. M. Alvarez, S. A. Harfenist, J. T. Khoury, T. G. Schaaff, P. W. Stephens, I. Vezmar, Z. L. Wang, A. Wilkinson, R. L. Whetten, unpublished.
[26] R. P. Andres, T. Bein, M. Dorogi, S. Feng, J. I. Henderson, C. P. Kubiak, W. Mahoney, R. G. Osifchin, R. Reifenberger, *Science* **1996**, *273*, 1690.
[27] A. P. Alivisatos, *J. Phys. Chem*. **1996**, *100*, 13 226.
[28] C. B. Murray, C. R. Kagan, M. G. Bawendi, *Science* **1995**, *270*, 1335.
[29] J. S. Yin, Z. L. Wang, unpublished.
[30] P. H. Hess, P. H. Parker, Jr., *J. Appl. Polym. Sci.* **1966**, *10*, 1915.
[31] K. Yamaguchi, K. Matsumoto, T. Fujii, *J. Magn. Soc. Jpn.* **1992**, *7*, 370.
[32] A. R. Thölen, *Acta Metall.* **1979**, *27*, 1765.
[33] J. R. Thomas, *J. Appl. Phys.* **1966**, *37*, 2914.
[34] C. H. Griffiths, M. P. O'Horo, T. W. Smith, *J. Appl. Phys.* **1979**, *50*, 7108.
[35] Y. D. Zhang, J. I. Budnick, *Appl. Phys. Lett.* **1997**, *70*, 1083.
[36] J. S. Yin, Z. L. Wang, *Phys. Rev. Lett.* **1997**, *79*, 2570.
[37] M. D. Bentzon, J. Van Wonterghem, S. Mørup, A. Thölen, C. J. W. Koch, *Philos. Mag. B* **1989**, *60*, 169.
[38] M. D. Bentzon, A. Thölen, *Ultramicroscopy* **1991**, *38*, 105.
[39] J. Van Wonterghem, S. Mørup, S. W. Charles, S. Wells, *J. Colloid Interface Sci.* **1988**, *121*, 558.
[40] I. Nakatani, M. Hijikata, K. Ozawa, *J. Magn. Magn. Mater.* **1993**, *122*, 10.
[41] *High Resolution Transmission Electron Microscopy and Associated Techniques* (Eds: P. Buseck, J. Cowley, L. Eyring), Oxford University Press, Oxford **1992**.
[42] L. Marks, *Rep. Prog. Phys.* **1994**, *57*, 603.
[43] T. S. Ahmadi, Z. L. Wang, T. C. Green, A. Henglein, M. A. El-Sayed, *Science* **1996**, *28*, 1924.
[44] Z. L. Wang, T. S. Ahmadi, M. A. El-Sayed, *Surf. Sci.* **1996**, *380*, 302.
[45] S. Ino, *J. Phys. Soc. Jpn.* **1966**, *21*, 346.
[46] J. G. Allpress, J. V. Sanders, *Surf. Sci.* **1967**, *7*, 1.
[47] P.-A. Buffat, M. Flüeli, R. Spycher, P. Stadelmann, J.-P. Borel, *Faraday Discuss.* **1991**, *92*, 173.
[48] A. Howie, L. D. Marks, *Philos. Mag. A* **1984**, *49*, 95.
[49] D. J. Smith, L. D. Marks, *J. Cryst. Growth* **1981**, *54*, 433. L. D. Marks, D. J. Smith, *J. Microsc.* **1983**, *130*, 249.
[50] P. M. Ajayan, L. D. Marks, *Phase Transitions* **1990**, *24*, 229.
[51] Z. L. Wang, J. Petroski, M. A. El-Sayed, unpublished.
[52] C. L. Cleveland, U. Landman, M. N. Shafigullin, P. W. Stephens, R. L. Whetten, *Z. Phys. D* **1997**, *40*, 503.
[53] C. L. Cleveland, U. Landman, T. G. Schaaff, M. N. Shafigullin, P. W. Stephens, R. L. Whetten, *Phys. Rev. Lett.* **1997**, *79*, 1873.
[54] M. M. Alvarex, J. T. Khoury, T. G. Schaaff, M. N. Shafigullin, I. Vezmar, R. L. Whetten, *Chem. Phys. Lett.* **1997**, *266*, 91.
[55] S. Murthy, Z. L. Wang, R. L. Whetten, *Philos. Mag. Lett.* **1997**, *75*, 321.
[56] J. O. Malm, M. A. O'Keefe, *Ultramicroscopy* **1997**, in press.
[57] Z. L. Wang, Z. C. Kang, *Functional and Smart Materials—Structural Evolution and Structure Analysis*, Plenum, New York **1997**.
[58] W. D. Luedtke, U. Landman, *J. Phys. Chem.* **1996**, *100*, 13 323.
[59] G. E. Poirier, E. D. Pylant, *Science* **1996**, *272*, 1145.
[60] S. Chiang, *Science* **1996**, *272*, 1123.
[61] D. J. Schiffrin, unpublished.
[62] C. Y. Yang, *J. Cryst. Growth* **1979**, *47*, 274, 283.
[63] S. Ino, *J. Phys. Soc. Jpn.* **1969**, *27*, 941.
[64] Z. L. Wang, *Elastic and Inelastic Scattering in Electron Diffraction and Imaging*, Plenum, New York **1995**.
[65] S. A. Harfenit, Z. L. Wang, in preparation.
[66] Z. Zhang, M. G. Lagally, *Science* 1997, *276*, 377.
[67] M. Yao, D. J. Smith, *J. Microsc.* **1994**, *175*, 252.
[68] J. S. Yin, Z. L. Wang, *J. Phys. Chem. B*, in press.
[69] A. Tonomura, *Electron Holography*, Springer, New York **1993**.
[70] H. Lichte, *Ultramicroscopy* **1986**, *20*, 293.
[71] A. K. Datye, D. S. Kalakkad, E. Vöikl, L. F. Allard, in *Electron Holography*, (Eds: A. Tonomura, L. F. Allard, G. Pozzi, D. C. Joy, Y. A. Ono), Elsevier, New York **1995**, 199.
[72] Y. Aharonov, D. Bohm, *Phys. Rev.* **1959**, *115*, 485.
[73] M. Mankos, J. M. Cowley, M. R. Scheinfein, *MRS Bull.* **1995**, *Oct.*, 45.
[74] T. Harayama, J. Chen, Q. Ru, K. Ishizuka, T. Tanji, A. Tonomura, *J. Electron Microsc.* **1994**, *43*, 190.
[75] Z. L. Wang, A. J. Shapiro, *Ultramicroscopy* **1995**, *60*, 115.
[76] D. H. Pearson, C. C. Ahn, B. Fultz, *Phys. Rev. B* **1993**, *47*, 8471.
[77] H. Kurata, C. Colliex, *Phys. Rev. B* **1993**, *48*, 2102.
[78] Z. L. Wang, J. S. Yin, Y. D. Jiang, J. Zhang, *Appl. Phys. Lett.* **1997**, *70*, 3362.
[79] Z. L. Wang, J. S. Yin, *Philos. Mag. B.* **1997**, in press.
[80] Z. L. Wang, J. S. Yin, W. D. Mo, Z. J. Zhang, *J. Phys. Chem. B* **1997**, *101*, 6793.
[81] C. P. Collier, R. J. Saykally, J. J. Shiang, S. E. Henrichs, J. R. Heath, *Science* **1997**, *277*, 1978.
[82] Z. L. Wang et al., unpublished data.

  0935-9648/98/0101-0030 $ 17.50+.50/0